BIOPHYSICS

Molecular organization and mechanics of single vimentin filaments revealed by super-resolution imaging

Filipe Nunes Vicente[1], Mickael Lelek[2], Jean-Yves Tinevez[3], Quang D. Tran[4,5], Gerard Pehau-Arnaudet[6,7], Christophe Zimmer[2], Sandrine Etienne-Manneville[4], Gregory Giannone[1], Cécile Leduc[4,5]*

Intermediate filaments (IFs) are involved in key cellular functions including polarization, migration, and protection against large deformations. These functions are related to their remarkable ability to extend without breaking, a capacity that should be determined by the molecular organization of subunits within filaments. However, this structure-mechanics relationship remains poorly understood at the molecular level. Here, using super-resolution microscopy (SRM), we show that vimentin filaments exhibit a ~49-nanometer axial repeat both in cells and in vitro. As unit-length filaments (ULFs) were measured at ~59 nanometers, this demonstrates a partial overlap of ULFs during filament assembly. Using an SRM-compatible stretching device, we also provide evidence that the extensibility of vimentin is due to the unfolding of its subunits and not to their sliding, thus establishing a direct link between the structural organization and its mechanical properties. Overall, our results pave the way for future studies of IF assembly, mechanical, and structural properties in cells.

INTRODUCTION

The cytoskeleton of all metazoan cells is mainly composed of three types of filaments: microtubules, actin filaments (F-actin), and intermediate filaments (IFs). Cytoplasmic IFs, which exclude lamins localized inside the nucleus, form a network that extends from the nucleus to the plasma membrane and work in coordination with the other cytoskeletal filaments to control key cellular functions, such as polarization, migration, division, and signaling (*1*–*3*). IF networks also stabilize cellular architecture and protect cells from severe stretching (*4*, *5*), confirming their mechanical role as cellular integrators described in the early literature (*6*). In particular, vimentin IF, a key marker of migrating mesenchymal cells, is essential for maintaining cell integrity and viability under conditions involving large deformations (*5*). This mechanical role was directly related to IFs interconnection with other cytoskeletal filaments and their synergetic ability to effectively disperse local deformations, allowing energy dissipation throughout the cell (*5*). The crucial role of IF is also highlighted by the fact that more than 90 human diseases are directly caused by mutations in IF proteins and that changes in IF composition also promote tumor growth and spreading (*7*).

Vimentin filaments exhibit assembly, structural, and mechanical properties that strongly differ from F-actin and microtubules and that are also less understood at the molecular level. In terms of assembly, vimentin filaments result from the passive self-assembly of nonpolar tetramers that associate laterally to form short filament precursors called unit-length filaments (ULFs), which then fuse longitudinally during filament elongation (*7*). Simultaneously, vimentin also intercalate subunits along their length (*8*–*10*). Cross-linking experiments have shown that complex rearrangement of tetramers occurs during filament maturation (*11*), but structural information about vimentin at the level of filament is missing (*12*). Cryo–electron microscopy (cryo-EM) images showed that vimentin filaments consist of four protofibrils with a right-handed supertwist and a helical pitch of ~96 nm, but the longitudinal positions of the tetramers within the protofibrils could not be distinguished (*13*). In terms of mechanical properties, vimentin filaments can be elongated up to 350% along their length without breaking, in contrast with F-actin and microtubules that tend to break or disassemble at moderate strain (*14*–*17*). This high extensibility was attributed to the reversible and cooperative unfolding of α-helices within vimentin subunits due to stochastic and numerical modeling (*14*, *16*). Internal sliding of the subunits would also be consistent with these experimental observations, but the spatial resolution of the experiments was not sufficient to observe the exact molecular mechanism (*16*). Furthermore, most experiments designed to characterize the properties of vimentin were performed on purified proteins reconstituted in vitro and thus overlooked the potential role of cellular processes. For example, posttranslational modifications occurring in the cytoplasm might modify the structural organization of IFs and, as a result, affect their assembly and mechanical properties (*18*). Overall, the structural organization of vimentin filaments and their structure-mechanics relationship remain unclear both in vitro and within cells, primarily due to the lack of experimental techniques to resolve the molecular organization of proteins and to investigate their response to forces.

By delivering images with spatial resolutions below the diffraction limit of light, super-resolution microscopy (SRM) techniques have created new opportunities to study the nanoscale architecture of cellular structures directly in cells (*19*, *20*). We used two major classes of SRM: (i) stochastic approaches based on single-molecule localization microscopy (SMLM), such as photoactivated localization microscopy (PALM) (*21*), stochastic optical reconstruction microscopy (STORM) (*22*, *23*), or DNA-based point accumulation for imaging in nanoscale topography (DNA-PAINT) (*24*), which typically achieve

[1]Institut Interdisciplinaire des Neurosciences, CNRS UMR 5297, Université de Bordeaux, Bordeaux F-33000, France. [2]Imaging and Modeling Unit, Institut Pasteur, CNRS UMR 3691, Paris F-75015, France. [3]Image Analysis Hub, 2RT / DTPS, Institut Pasteur, Paris F-75015 , France. [4]Cell Polarity, Migration and Cancer Unit, Institut Pasteur, CNRS UMR 3691, équipe labellisée Ligue contre le cancer, Paris F-75015, France. [5]CNRS UMR 7592, Institut Jacques Monod, Université de Paris, Paris F-75013, France. [6]CNRS UMR 3528, Institut Pasteur, Paris F-75015, France. [7]Ultrastructural BioImaging Platform, Institut Pasteur, Paris F-75015, France.
*Corresponding author. Email: cecile.leduc@ijm.fr

the best resolution; and (ii) selective deactivation of fluorophores by stimulated emission, minimizing the cross-sectional area of the focal spot below the diffraction limit, such as stimulated emission-depletion (STED) microscopy (*25*). SMLM-based techniques allow deciphering, for example, the structural organization of integrin-based adhesions (*26*, *27*) or nuclear pore complexes (*28*) at the nanoscale. The recent development of a cell-stretching device compatible with SRM methods, including SMLM, enables the exploration of protein deformation or reorganization upon mechanical strain (*29*). This technique also enables the study of the molecular mechanisms involved in mechanosensitivity directly inside cellular structures (*29*).

Here, we used SRM techniques to reveal the organization of vimentin filaments at the molecular scale directly inside cells and in vitro and bring new important insights into the IF assembly mechanism. Furthermore, by combining IF stretching with SRM, we showed the impact on external forces on the molecular organization of the filaments and unveiled their structure-mechanics relationship. This established a novel strategy to assess the tension applied on vimentin filaments in cells by quantifying their structural organization. Together, our results open the way to a better understanding of the structural, assembly, and mechanical properties of IF in cells.

RESULTS

Vimentin ULFs are made of parallel tetramers inside cells

To probe the molecular organization of vimentin filaments directly inside cells, we first studied the early stage of filament assembly and focused on vimentin ULFs using direct STORM (dSTORM) (*23*). ULFs are known to result from the lateral association of 8 to 10 tetramers, which are themselves made of the antiparallel association of parallel dimers (Fig. 1A) (*7*). Cross-linking experiments have shown that ULFs reconstituted in vitro are predominantly made of A11 tetramers in which there is an N-terminal overlap of the two antiparallel dimers (Fig. 1A) (*11*). The alternative types of tetramers—A22 in which there is a C-terminal overlap of the two antiparallel dimers and A12 made of in-register antiparallel dimers (fig. S1A)—were only found in mature filaments (*11*). However, whether the ULF organization is similar in cells or whether the cellular environment alters IF assembly has not been reported. To study ULFs in cells, we took advantage of the vimentin mutant vimentin-Y117L, which impairs longitudinal end-to-end annealing of filaments and thus stops filament assembly at the ULF stage (*30*, *31*). The ULFs have previously been shown to form particles in cells and exchange subunits with the soluble tetrameric pool in an adenosine triphosphate–dependent manner (*32*). Vimentin-Y117L–green fluorescent protein (GFP) was expressed in mouse embryonic fibroblast (MEF) vimentin knockout (KO) completely depleted of cytoplasmic IFs (*30*, *31*). The GFP-terminal ends were labeled with GFP-nanobodies labeled by Alexa Fluor 647 (GFP-nanobodies-AF647), which are fluorescently labeled single-chain antibody domains with high affinity for GFP that are widely used for SRM (*33*). With the absence of unlabeled endogenous vimentin, the labeling of vimentin was maximized allowing us to perform quantitative dSTORM imaging under optimal conditions (*23*, *34*). We performed two-dimensional (2D) dSTORM imaging of fixed cells (Fig. 1B and fig. S2A). While only large dots were observed in the GFP channel with epifluorescence, 2D dSTORM images showed that the vimentin C-terminal ends formed doublets within the ULFs, consistent with ULFs being made of tetramers organized in a parallel fashion in cells. We estimated the spatial resolution of the images by measuring the full width at half maximum of all the doublet dots and found 27 nm on average (SD, 10 nm). The distance between the C-terminal ends, hereafter called pairwise distance, was quantified using a double Gaussian fit (Fig. 1C) and found to be ~50 nm on average (SD, 14 nm) (Fig. 1D). This distance is significantly smaller than the ULF length of ~60 nm measured in vitro using EM (*35*, *36*).

To understand the discrepancy between the ULF length measured in vitro with EM and in cells, we first investigated whether this difference was due to the GFP location or size. Vimentin proteins are divided in three parts: a central α-helical rod domain flanked by two non–α-helical end domains, a head in N-terminal, and a tail in C terminus (Fig. 1A). Because the GFP tag is localized at the end of the disordered tail domain, its relative position to the end of the rod domain is not clearly defined. Vimentin tails may swivel around the end of the rod domain and thereby affect the measurements of the distance between the C-terminal ends. To test this hypothesis, we reduced the size of the tag by replacing the GFP with a 12–amino acid tag, called "Spot" (*37*), inserted between the rod and the tail (Fig. 1E). We expressed the vimentin-Y117L-Spot-Tail construct in MEF vimentin KO cells, fixed them, and performed immunolabeling with AF647-labeled Spot nanobodies (Spot-nanobodies-AF647) to perform 2D dSTORM images (Fig. 1E). As found with GFP, ULFs also appeared as dots in epifluorescence images and doublets in 2D dSTORM images, with an average length of ~50 nm (Fig. 1D). The absence of a significant difference for doublet size measured with C-terminal GFP-tagged vimentin and vimentin with a Spot tag between the rod and tail confirms that probe size and vimentin tail have no impact on ULF length measurement.

To further investigate the length discrepancy, we tested whether other types of tetramers than A11, such as A22 and A12 (fig. S1A), could form in cells. To do so, we quantified the localization of vimentin N-terminal heads within ULFs (Fig. 1A). We designed a Spot-vimentin-Y117L construct that was expressed in MEF vimentin KO cells and performed 2D dSTORM imaging (Fig. 1F). We observed that vimentin heads were also organized in doublets within ULFs, but we measured a significantly smaller doublet length of ~34 nm (SD, 13 nm) compared to C-terminal ends. These results are consistent with an organization of vimentin tetramers with C-terminal ends on the outside and N-terminal ends on the inside of ULFs and thus indicate that ULFs are predominantly composed of A11 tetramers in cells. We confirmed the predominance of A11 type over A22 and A12 structural organization by simultaneously observing vimentin heads (labeled by a Spot tag) and tails (labeled by a GFP) using dual-color STED imaging of Spot-nanobodies-AF594 (Alexa Fluor 594–labeled Spot nanobodies) and GFP-nanobodies-Star635 (Star635-labeled GFP-nanobodies) (fig. S1B).

Vimentin ULFs are ~59 nm long and are tilted in cells

We then investigated whether the discrepancy between ULF length measured in vitro with EM and in cells with 2D dSTORM could result from tilted ULFs projected in 2D. We used a 3D dSTORM microscope equipped with two objectives and two cylindrical lenses, which allows for improved spatial resolution in all three dimensions (< 25 nm in each direction), compared to a single cylindrical lens combined with one objective (*38*). These experiments showed that ULFs were tilted in cells. The vimentin tails formed doublets, whose orientation could be quantified with an average angle of ~22° (SD,

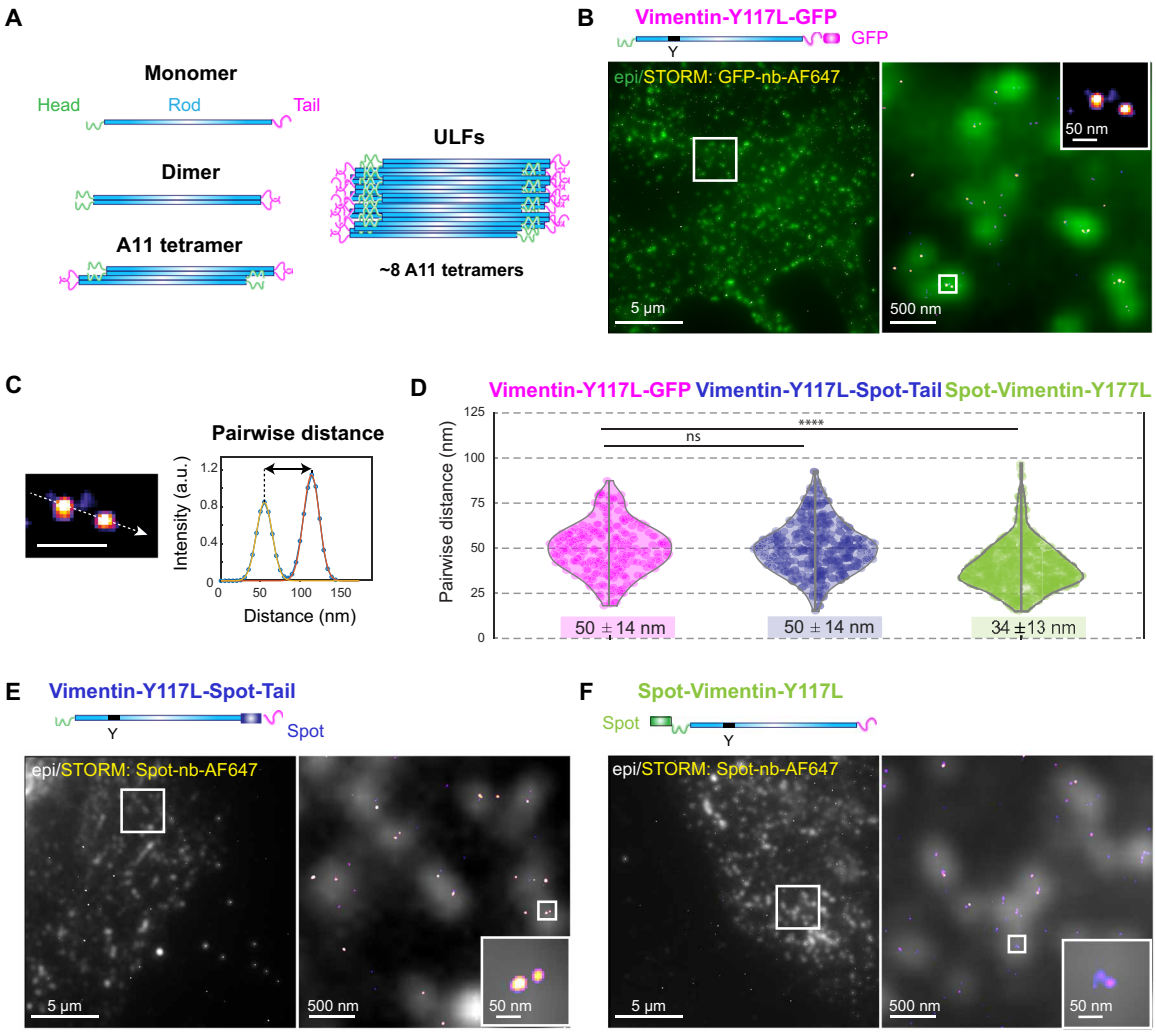

Fig. 1. Structural organization of vimentin ULFs in cells. (**A**) Schematic of vimentin assembly. Vimentin monomers are formed by a head (green), a rod (blue), and a tail (purple). Two parallel dimers associate to form antiparallel, half-staggered tetramers. About eight tetramers associate laterally to form vimentin precursors called ULFs. (**B**) Top: Schematic of the Vimentin-Y117L-GFP protein. Bottom: Epifluorescence image and a higher magnification the boxed region of an MEF vimentin KO cell expressing the vimentin-Y117L-GFP construct (green) superimposed on the corresponding 2D dSTORM image (fire) acquired with GFP-nanobodies-AF647 (GFP-nb-AF647). Inset: Magnifications of the boxed region. (**C**) Magnification of a ULF from the inset in (B). The fluorescence intensity profile along the ULF is fit by two Gaussian, and pairwise distance is calculated from the distance between the two peaks. a.u., arbitrary units. (**D**) Distributions of pairwise distances measured with the vimentin-Y117L-GFP (magenta), vimentin-Y117L-Spot-Tail (blue), and Spot-vimentin-Y117L (green) constructs expressed in MEF vimentin KO cells. Mean values ± SD of the total distributions are written below the violin plots. Data represent 253, 317, and 596 ULFs, respectively, collected from 9, 10, and 16 cells from three to four independent experiments. *P* value was calculated with a nested *t* test of the three repeats, ****$P < 0.0001$. n.s., not significant. (**E** and **F**) Top: Schematic of the Vimentin-Y117L-Spot-Tail protein (E) and Spot-Vimentin-Y117L protein (F). Bottom: Epifluorescence image (gray) and a higher magnification of the boxed region superimposed on the corresponding 2D dSTORM image (fire) of Spot-nanobodies-AF647 (Spot-nb-AF647) (fire). Inset: Magnifications of the boxed regions.

17°) relative to the horizontal, a value that is underestimated since the population of vertical ULFs could not be detected using our analysis method (Fig. 2, A to C). Two populations of orientation were observed: ~46% of ULFs had an angle of less than 15° (Fig. 2C), which could correspond to the population of ULFs aligned with the microtubule network almost parallel to the plasma membrane (fig. S3) (*39*) and the other population, with a higher tilt value, which could then correspond to "isolated" ULFs with a random orientation. To test this hypothesis, we quantified the ULF length distribution and orientation after microtubule disassembly induced by nocodazole treatment. While the ULF orientation became more uniformly distributed compared to untreated control cells (Fig. 2D), neither the mean ULF 3D length nor the 3D width of the distribution was significantly altered by microtubule depolymerization (Fig. 2D). The 2D projected doublet size was significantly shorter than in control (Fig. 2D), as observed in 2D dSTORM experiments (fig. S4), due to the loss of ULF orientation after microtubule depolymerization. These results also indicate that microtubule-associated motors do not alter the length of ULFs in cells. Inhibition of myosin II activity by blebbistatin did not affect ULF length distribution in 2D (fig. S4), suggesting that actin-associated motors do not alter ULF orientation and length. Taking into account the 3D coordinates, the doublet size was measured to be on average of 59 nm (SD, 15 nm) (Fig. 2D), in agreement with ULF length measured in vitro (*35*, *36*).

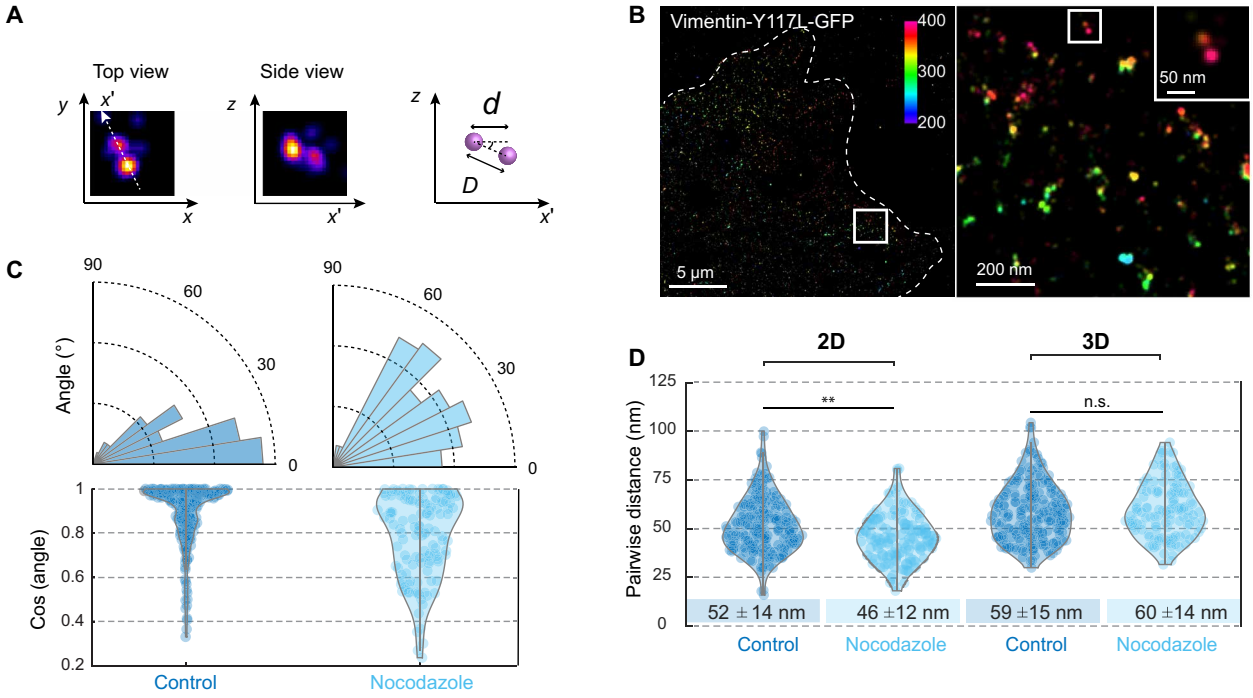

Fig. 2. Vimentin ULFs are ~59 nm long and are tilted in cells. (**A**) Top and side views of a ULF imaged by 3D dSTORM and a cartoon showing the projected distance "*d*" measured in 2D dSTORM, the real distance "*D*" between vimentin-Y11L-GFP C-terminal ends in ULFs measured in 3D, and the tilt angle. (**B**) 3D dSTORM image and a higher magnification of the boxed region of an MEF vimentin KO cell expressing vimentin-Y117L-GFP and labeled with GFP-nanobodies-AF647. The color indicates the depth *z* in nanometers. Inset: Magnification of the boxed region showing a ULF. Images were acquired using a dual-objective microscopy setup with cylindrical lenses (see Materials and Methods). (**C**) Distributions of ULFs angles relative to the substrate and cosinus of ULF angles in control cells and in cells treated with nocodazole. (**D**) Distributions of pairwise distances between vimentin-Y11L-GFP C-terminal ends in ULFs projected in 2D (distance "*d*") and measured in 3D (distance "*D*") in control and nocodazole-treated MEF vimentin KO cells. Mean values ± SD of the total distributions are written below the violin plots. ULFs (204 and 133) were analyzed from four control cells and five cells treated with nocodazole, respectively, acquired during two independent experiments. *t* test, $^{**}P < 0.01$.

We then corrected the distance between N-terminal ends for projection error and found a distance of ~39 nm. Our results unambiguously demonstrate that the length and structural organization of cellular ULFs, made up mostly of A11 tetramers, are similar to the ones reported in reconstituted systems (*11*, *35*, *36*) and that the orientation of ULFs in cells is determined by their interaction with the microtubule network, but not their length.

Vimentin ULF length is heterogeneous in cells

The distribution of pairwise distances between C-terminal tails, which we use as an estimate of ULF length, is broad around the mean value of 59 nm with an SD of 15 nm, i.e., ~25% of the mean length. This broad distribution could either result from uncertainties in the SRM measurements or could be intrinsically associated with the molecular organization of the ULFs since we ruled out the impact of the tail, the probe size, and position, as well as of any previous stretching by molecular motors (Figs. 1, D and E, and 2D). To quantify the possible errors coming from SRM measurements, we measured the nuclear pores radius, which has become a standard for quantitative SRM (*34*), using a similar labeling technique (imaging of Nuclear pore complex proteins 96 (Nup96-SNAP) labeled with SNAP–Alexa Fluor 647), the same 3D dSTORM microscopy setup and quantification method (fig. S5). We measured a nuclear pore radius of 58 nm (SD, 6 nm) with a narrower distribution, indicating that the width of the distribution for vimentin ULF lengths is not inherent to the imaging technique. Moreover, we did not observe any correlation between ULF length and the mean peak intensities of the doublet (Pearson correlation coefficient of 0.1 and *P* value for the nonzero correlation hypothesis of 0.3), suggesting that the length heterogeneity is not related to fluctuations in the number of tetramers forming the ULF (fig. S6). Together, these results show that the length of vimentin ULFs is intrinsically heterogeneous in cells, which may affect the regularity of filament organization after assembly.

The organization of vimentin tails exhibits an axial repeat of 49 nm within filaments in cells

The internal organization of mature vimentin filaments is still poorly understood since the exact organization of tetramers within the filaments is unclear (*12*). It was previously shown in biochemical studies that while ULFs consist mainly of A11-type tetramers, mature vimentin filaments also contain A22- and A12-type tetramers in addition to the A11 (fig. S1A), suggesting that major rearrangements of tetramers occur during longitudinal annealing of filaments (*11*). Since the commonly accepted mechanism for filament assembly is the fusion of vimentin ULFs, we investigated whether we could observe a signature of this organization by quantifying the position of the head and tail domains in mature filaments using SRM. We first used a vimentin construct with a C-terminal GFP expressed in MEF vimentin KO cells and labeled with GFP-nanobodies-AF647 and performed 2D dSTORM images of vimentin filaments in the total internal reflection fluorescence (TIRF) mode (Fig. 3A). We clearly observed an axial repeat along the filaments, reflecting

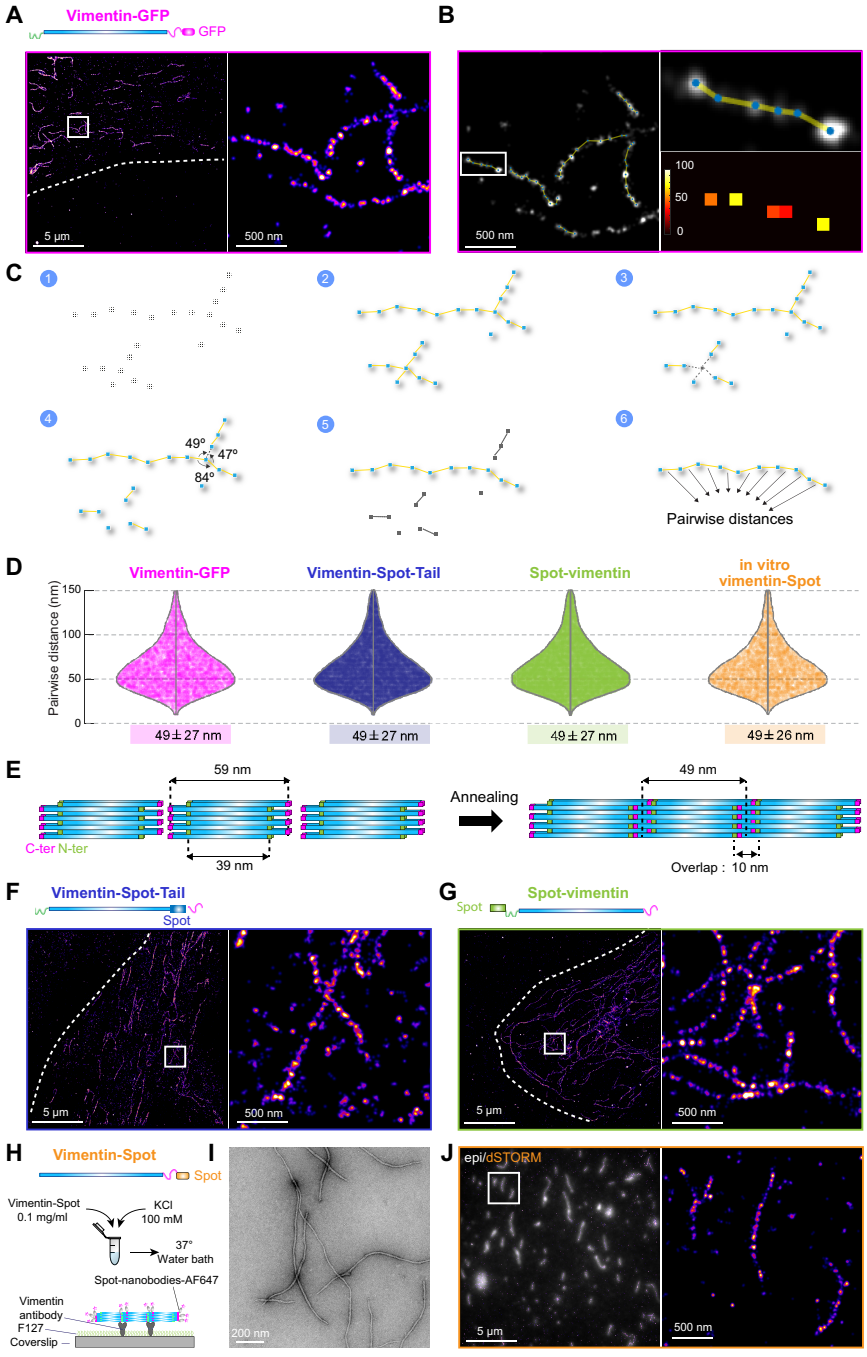

Fig. 3. Structural organization of vimentin filaments in cells and in filaments reconstituted in vitro. (**A**) 2D dSTORM image and a higher magnification of the boxed region of an MEF vimentin KO cell expressing vimentin-GFP and labeled with GFP-nanobodies-AF647. Dashed line indicates the cell edge. (**B**) Schematics of a filament and how pairwise distances are measured. Left: 2D dSTORM image from (A) superimposed with intensity peaks, which are automatically detected (labeled in blue) and with the distances to the closest neighbors depicted in yellow (see Materials and Methods). Right: Zoom of the boxed area and color map of the pairwise distances. (**C**) Schematics of the analysis method for the pairwise distance measurements (see Materials and Methods). (**D**) Distributions of pairwise distances between vimentin-GFP tails (magenta), vimentin-Spot-Tails (blue), and Spot-vimentin heads (green) measured in cells and vimentin-Spot tails (yellow) measured in in vitro reconstituted filaments. A total of 4664, 13,936, and 15,903 pairwise distances were measured respectively from 10 cells per condition acquired in each case in three independent experiments, and 4167 pairwise distances were quantified from three independent experiments for reconstituted filaments. The distribution modes and SDs are written below the violin plots. (**E**) Schematic of the intertwining of ULFs after end-to-end annealing. (**F** and **G**) 2D dSTORM image and a higher magnification of the boxed region of MEF vimentin KO cells expressing vimentin-Spot-Tail (F) and Spot-vimentin (G) and labeled with Spot-nanobodies-AF647. Dashed line indicates cell edges. (**H**) Protocol of vimentin-Spot filament assembly. After dialysis in a 2.5 mM phosphate buffer, vimentin assembly is started by addition of KCl (final concentration of 100 mM) to vimentin tetramers (0.1 mg/ml) and incubation for 3 hours at 37°C. (**I**) Representative transmission EM image of vimentin-Spot filaments assembled in vitro. (**J**) Epifluorescence images (gray) superimposed on the corresponding 2D dSTORM images (fire) of vimentin-Spot filaments. Right: 2D dSTORM image of the boxed region.

the organization of the vimentin tails. We developed an image analysis software (see Materials and Methods) that allows automatic detection of intensity peaks and measurement of the pairwise distance between peaks along the filaments (Fig. 3, B and C). The distribution of pairwise distances between the vimentin tails shows a maximum at ~49 nm, which we take as an estimate of the axial repeat (Fig. 3D). Because the observed filaments were a few micrometers long and localized in a layer of less than 100 nm above the surface in the TIRF mode, their tilt angle was less than 5°, and the error on the axial repeat estimation was less than 0.4%. The 3D dSTORM images also confirmed that most filaments were parallel to the glass surface (fig. S7). We also verified that this organization was not cell specific and that cell fixation had no impact on the axial repeat measurements and nor did microtubule depolymerization (figs. S8 to S9). SRM reveals the structural organization of mature vimentin filaments, which display a ~ 49-nm axial repeat of the tails, demonstrating that the filaments are made up of a succession of ULFs (Fig. 3E).

Next, we tested whether the size and localization of the GFP tag could affect the estimation of the axial repeat along the filaments by 2D dSTORM of a vimentin-Spot-Tail construct (Fig. 3F). The distribution of pairwise distances showed no significant difference compared with that obtained with vimentin-GFP, showing that neither the tag size nor tail swiveling had any impact on the axial repeat (Fig. 3D). Because the vimentin tail has also been implicated in vimentin organization and remodeling in many cell types (*2*), we tested whether tail-less vimentin displayed similar organization using a construct vimentin-ΔTail-Spot, but we also did not find any significant difference in the axial repeat with vimentin-GFP (fig. S9, A and B). Last, we also showed that a similar axial repeat of vimentin tails was present in endogenous IF network in astrocytoma cells after 2D dSTORM imaging of vimentin tails, using site-specific labeling via a monoclonal antibody targeting an epitope on the tails (clone V9) (fig. S9, C and D). This indicates that the characterized structural organization of vimentin is not an artifact due to overexpression of vimentin proteins. These results show that the organization of vimentin tails display an axial repeat of ~49 nm along the filaments in cells, which is smaller than the 59 nm measured in ULFs (Fig. 2D). This is quantitatively consistent with a scenario where ULFs partially overlap by ~10 nm during the end-to-end annealing process of filament assembly and without major structural reorganization of the ULFs (Fig. 3E). If the spatial resolution of the system was less than 10 nm, then we would expect an alternation of 39 and 10 nm of the tails due to this partial overlap of ULFs (Fig. 3E). With a resolution of ~27 nm, the tails of successive overlapping ULFs ends (10 nm apart) appear as single spots, leading to an axial repeat of 49 nm.

Vimentin filaments intertwine during the fusion process leading to filament assembly

To further validate this scenario of ULF intertwining, we investigated the organization of vimentin heads within filaments in cells using the N-terminal Spot tag and 2D dSTORM imaging of Spot-nanobodies-AF647 (Fig. 3G). We observed a distribution of pairwise distances similar to that of vimentin tails with a main peak also at ~49 nm (Fig. 3D). Although longer than the distance between vimentin heads in ULFs that we estimated to be ~39 nm (Figs. 2D and 3E), this axial repeat is still compatible with the picture that ULFs partially overlap during the annealing process. In principle, we would expect an alternation of 39 and 10 nm for the N-terminal heads (Fig. 3E), but the SRM setup does not have the spatial resolution to resolve this pattern. As in the case of vimentin tails, the heads of consecutive overlapping ULF ends appear as single spots leading to a global axial repeat of 49 nm. Overall, our results allow us to provide strong evidence of ULFs intertwining during filament assembly and to estimate of the overlap distance of ULFs directly inside cells.

Vimentin structural organization is similar in in vitro reconstituted filaments and in cells

Since previous studies on vimentin have been performed with filaments reconstituted in vitro, we tested whether the filament organization we found in cells was similar in vitro. We designed a vimentin construct with a Spot tag at the C-terminal end and purified it from bacteria following a previously described protocol (*40*). The reconstituted filaments were assembled by addition of salt (Fig. 3H). Using EM, the Spot tag was checked to have no impact on the formation of filaments (Fig. 3I). Then, we performed 2D dSTORM imaging of nonfixed filaments attached on a glass surface via anti-vimentin antibodies and immunostained with Spot-nanobodies-AF647 (Fig. 3, H to J). The distribution of pairwise distances between vimentin tails displayed an axial repeat of ~49 nm and did not exhibit significant differences with that observed inside the cell (Fig. 3D). We also verified that in vitro ULFs, obtained after 2 s of assembly, had a similar structural organization and length than in cells (fig. S2B). Together these results show that the internal organization of filaments in vitro and inside the cell are similar, suggesting that interactions with cellular proteins have a limited impact on vimentin architecture. The 49-nm axial repeat of the tails can therefore be used as a "ruler" for vimentin filaments.

Mechanical forces exerted on reconstituted filaments increase the axial repeat

Vimentin filaments have remarkable mechanical properties as they can be stretched in vitro (*14*–*17*). Two molecular mechanisms are, in principle, consistent with the extensibility of single filaments: either unfolding of the α-helices or the sliding of tetramers within the filaments (*14*, *16*). We studied the impact of single-filament stretching on the axial repeat to decipher which molecular mechanism is involved. We used a stretching device compatible with all the SRM techniques that was used to study mechanosensing in cells (*29*). We directly attached the reconstituted filaments to the stretchable polydimethylsiloxane (PDMS) substrate using anti-vimentin antibodies, as on glass, and applied a uniaxial stretching step of 30% amplitude, which increased the contour length of the filaments by ~18% (averaged for all the directions) (Fig. 4, A and B). We performed 2D dSTORM images of vimentin tails labeled by Spot-nanobodies-AF647 without or with stretching (Fig. 4B) and computed the pairwise distances parallel (0° ± 10°) and perpendicular (90° ± 10°) to the stretch axis. We observed a significant increase in pairwise distances parallel to the stretching axis compared to perpendicular distances, which was not present in the control experiment performed on the stretching device but without stretching (Fig. 4, C to E). Although the frequency of pairwise distances around 64 nm, corresponding to a 30% increase compared to the case without stretching, was higher in the parallel case (Fig. 4D), the maximum of the distribution was shifted by only ~5 nm, suggesting that not all subunits are unfolded during stretching. Our results thus provide direct evidence that vimentin subunits change conformation during stretching and also give fundamental insights into the link between molecular architecture and mechanical properties of single filaments. In

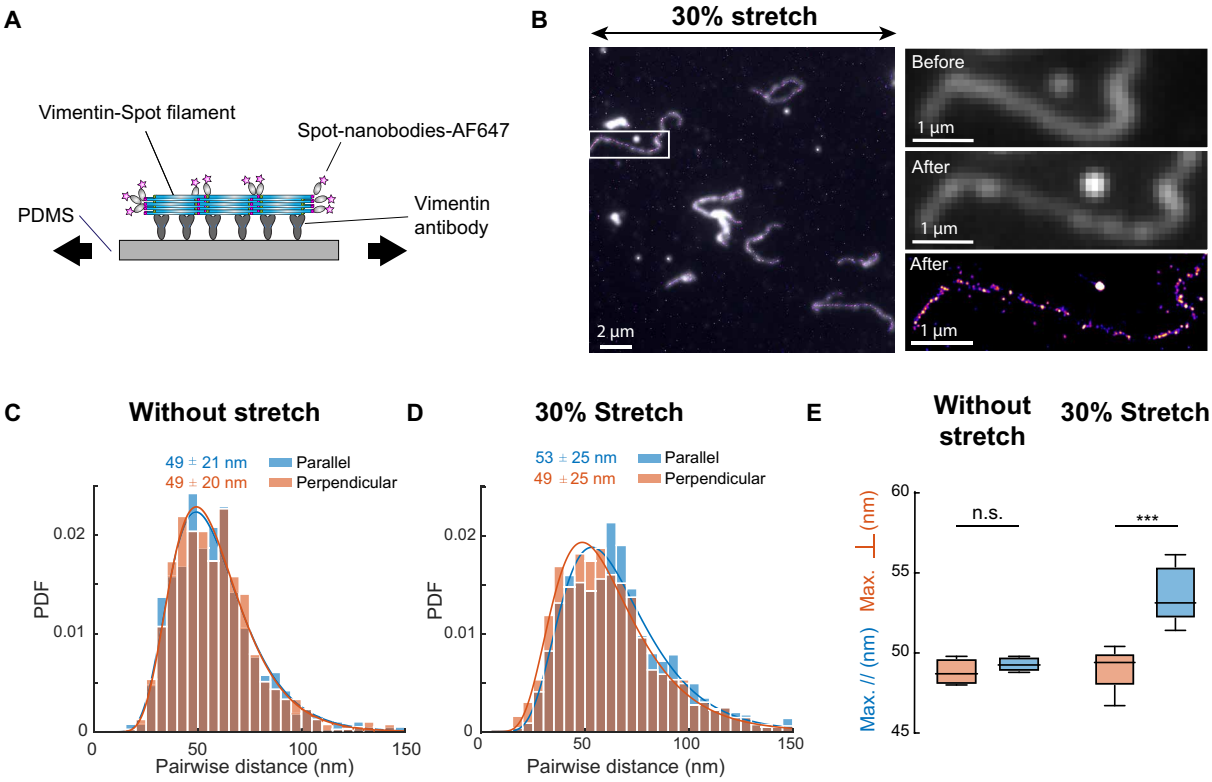

Fig. 4. Structural organization of stretched vimentin filaments reconstituted in vitro. (**A**) Schematic of vimentin-Spot filament attachment to the PDMS subtract through vimentin antibodies and immunolabeled by Spot-nanobodies-AF647. The subtract is passivated by bovine serum albumin (BSA). (**B**) Epifluorescence images (gray) superimposed on the corresponding 2D dSTORM images (fire) of vimentin-Spot filaments stretched 30%. Right: Higher magnification of the boxed region before and after stretching (epi and dSTORM). (**C** and **D**) Histograms of pairwise distances aligned with the uniaxial stretch (parallel, blue) and perpendicular to the stretch direction (perpendicular, orange) before stretch (C) and for a stretch of 30% (D). PDF, probability density function. Blue and orange curves correspond to a lognormal fit. The distribution modes and SDs are written above the curves. A total of 753 parallel and 779 perpendicular pairwise distances were measured before stretching, and 1755 parallel and 1452 perpendicular pairwise distances were measured after 30% stretch, acquired from three independent experiments. No significant difference was observed between the parallel and the perpendicular distributions before stretching, and a **** difference was observed for the 30% stretch condition ($P < 0.0001$). (**E**) Box and whiskers (minimum to maximum) of the modes of the lognormal fit of the pairwise distances parallel (blue) and perpendicular (orange) to the stretch direction. Four dSTORM images were analyzed before stretch and five after 30% stretch from three independent experiments. Paired *t* test was used to compare the two conditions. ***$P < 0.001$.

addition, these results also reveal that pulling on filaments induces an increased distance between vimentin tails, indicating that the axial repeat length may be taken as a readout of the tension applied on the filaments.

Vimentin filaments are not elongated after cell stretching up to 50%

Last, we studied the impact of cell stretching on the axial repeat directly in cells. We applied a step of uniaxial stretch up to 50% amplitude to live cells using the stretching device compatible with SRM, followed by immediate fixation of the cell after having reached the stretching plateau (in less than 1 min). First, we used MEF vimentin KO cells expressing vimentin-GFP and plated them on the fibronectin-coated stretchable PDMS substrate. Low-resolution epifluorescence images of vimentin-GFP allowed us to observe the reorganization of the vimentin network axis before and after stretching (Fig. 5A). Comparison of the mean directionality of the filaments before and after having reached the stretching plateau showed that the filaments reoriented along the stretching axis, attesting that external forces were transmitted to the filaments (Fig. 5B). We also quantified the extension of single filaments before and after stretching and observed that the length increase was less than 6% on average along the stretch axis and for a stretch amplitude of up to 50% (Fig. 5C). Next, we analyzed the structural organization of vimentin filaments using DNA-PAINT with a HALO tag at the C-terminal end of vimentin, as previously described (*29*). The DNA-PAINT method uses the stochastic binding of a fluorescent ligand to localize the target protein. DNA-PAINT is based on hybridization of complementary DNA strands, one located on the target protein (docking strand) and the other one on the dye (imager strand) (*24*). We switched from dSTORM of vimentin-GFP to DNA-PAINT with vimentin-HALO to further improve the quality of the images. We analyzed the pairwise distance between vimentin tails and quantified the axial repeat with or without stretching. Comparison between pairwise distances parallel (0° ± 10°) and perpendicular (90° ± 10°) to the stress axis did not show any significant difference for 35 and 50% stretch, and no difference was observed with control cells that were not stretched (Fig. 5, D to G, and fig. S10). The lack of significant filament extension or change in the internal organization of vimentin within the filaments indicates that cytoplasmic vimentin filaments are not under tension inside the cells, even after having reached a 50% stretch, or that they quickly release the applied tension.

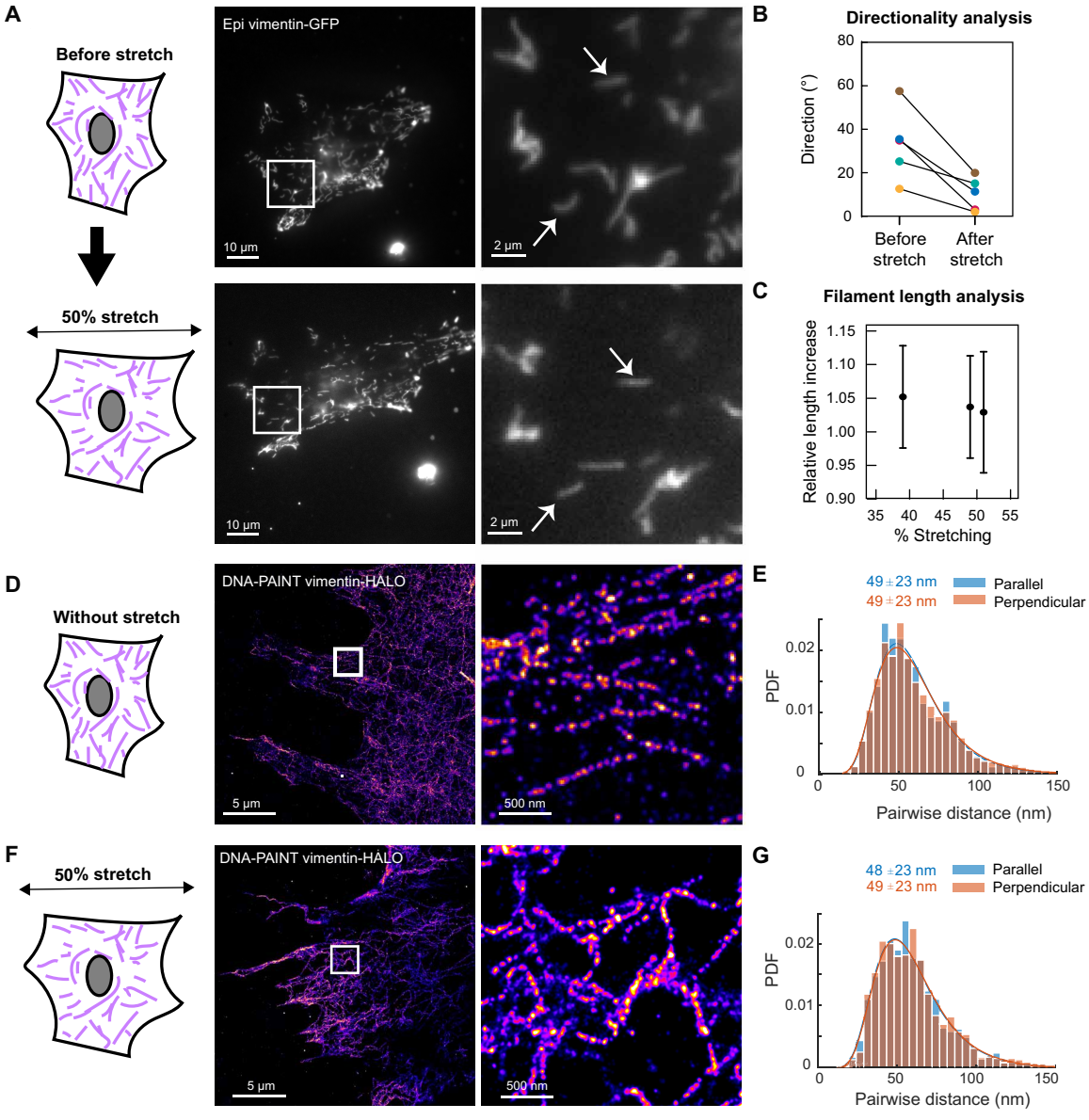

Fig. 5. Structural organization of vimentin filaments within stretched cells. (**A**) Epifluorescence images of an MEF vimentin KO cell expressing vimentin-GFP before and after 50% uniaxial stretch and higher magnification of the box regions. White arrows, filaments that are not stretched in the cell. (**B**) Directionality analysis performed using the Fiji plugin was performed before and after stretching of five cells. Zero degrees corresponds to the direction parallel to the stretch axis. (**C**) Relative length increase measured in three live cells after 39 to 51% stretch. (**D**) DNA-PAINT image of an MEF vimentin KO expressing vimentin-HALO and stretched 50%. Middle: Magnification of the boxed region. Right: Corresponding map of pairwise distances. (**E**) Histogram of pairwise distances aligned with the uniaxial stretch (parallel, i.e., with an angle of 0° ± 10°, blue) and perpendicular to the stretch direction (perpendicular, i.e., with an angle of 90° ± 10°, orange), detected from the DNA-PAINT image in (D) (stretch 50%). Blue and orange curves correspond to a lognormal fit. The distribution modes and SDs are written above the curves. A total of 3823 and 4157 pairwise distances were measured respectively from two independent experiments. No significant difference was observed between the parallel and perpendicular distributions. (**F**) Left: DNA-PAINT image of an MEF vimentin KO expressing vimentin-HALO and not stretched. Middle: Magnification of the boxed region. Right: Corresponding map of pairwise distances. (**G**) Histogram of pairwise distances aligned with the uniaxial stretch (parallel, blue) and perpendicular to the stretch direction (perpendicular, orange) in a control cell without stretching (stretch 0%). Blue and orange curves correspond to a lognormal fit. The distribution modes and SDs are written above the curves. A total of 1242 and 1016 pairwise distances were measured, respectively, from two independent experiments. No significant difference was observed between the parallel and the perpendicular distributions.

DISCUSSION

Although vimentin IFs play a crucial role in many key cellular functions, such as mechanical integrity, polarization and invasion, our understanding of their structural organization is much more limited compared to F-actin or microtubules. Here, using site-specific labeling and SRM, we unveiled the architecture of vimentin filaments at the molecular level directly inside the cell and in reconstituted filaments in vitro. We showed that vimentin ULFs are mostly composed of A11 tetramers with a mean length of ~59 nm, with a broadly distributed size in cells. We then analyzed the organization of vimentin proteins within mature filaments both in cells and in reconstituted filaments. In both cases, the filaments showed an axial

repeat of ~49 nm in the organization of head and tail domains, consistent with a mechanism where the ends of vimentin ULFs intertwine during filament assembly. Last, using a stretching device compatible with SRM, we probed the impact of external stretching on the structural organization of filaments both in vitro and within cells. In the case of purified filaments, the axial repeat was increased for stretching amplitudes up to 30% only in filaments parallel to the stretch axis. This indicates that mechanical strain leads to the unfolding of α-helices in vimentin subunits. The axial repeat of intracellular filaments and their contour length did not increase in cells stretched up to 50%. Instead, the filaments reoriented in the direction of the stretch, indicating that the filaments were not under tension or that they released it quickly.

Starting with vimentin ULFs, we observed using SRM that the distribution of distances between C-terminal ends was broad (SD, 15 nm), reflecting the ULF polymorphism and size heterogeneity in cells. Because tetramers have been reported to be loosely packed within the ULFs (*41*), the size heterogeneity could also reflect a partial misalignment of the tetramers. It may not only be related to the variety of the ULF types, which are mostly formed of A11 tetramers, but could also include A22 or A12 tetramers (fig. S1B). In addition, using an improved 3D dSTORM imaging with 25-nm resolution in all three dimensions, we showed that the 3D information should not be overlooked. It provides crucial knowledge on the ULF orientation that may be important in the assembly process. One remaining question is whether the different types of ULFs could anneal during filament assembly and whether the type of ULF affects the assembly rate. Polymorphism after IF assembly has previously been described in terms of tetramer types and the number of tetramers per unit length (*7*) but only for filaments reconstituted in vitro. Here, we go one step further by describing this polymorphism directly inside the cell. We observed that the axial repeat reflecting the succession of ULFs within filament is also heterogeneous, which suggests that ULFs of different sizes may anneal together. Improvement of live SRM techniques will be necessary to achieve a better spatial and temporal resolution in 3D to study the dynamic assembly of filaments within cells and to understand the potential functions associated with this polymorphism. Moreover, resolving the sub-ULF organization within filaments will require the use of SRM technique having a resolution close to 1 nm, such as MINFLUX (*42*).

Our results brought significant advances in the understanding of vimentin structural organization and assembly. A previous study based on theoretical modeling of cross-linking experiments estimated the size of the axial repeat to be 42.7 nm (*43*). However, there was no direct experimental measurement of this length. Using SRM, we showed that the size of the axial repeat is ~49 nm. As ULFs in cells measure 59 nm, this demonstrates a partial ULFs overlap (~10 nm) occurring during filament assembly (*40*). Thus, our results provide direct evidence of the ULF intertwining within filaments, validating previous theoretical predictions (*43*). The intertwining of ULFs does not hinder the addition and removal of subunits along the filaments as observed in cells and in vitro (*8*–*10*), suggesting that the bond between tetramers can be broken spontaneously. Notably, 49 nm is also half the helical pitch of vimentin filaments measured by cryo-EM (*13*), suggesting that the helical pitch is formed by two successive ULFs. However, we do not have the spatial resolution with SRM to resolve the protobribils within filaments and measure the tilt orientation of these protofibrils with respect to the main axis of the filament. Cryo-EM and SRM therefore bring complementary descriptions of vimentin architecture. While cryo-EM resolve the protofibril organization and describes their helical path, SRM describes the size of the ULF after insertion within filaments regardless of the orientation of the protofibrils within the filament, and this is not accessible by cryo-EM since vimentin head and tail positions could not be distinguished with this technique. We also showed that vimentin filaments in cells and reconstituted in vitro displayed similar axial repeat, suggesting that the molecular organization of IFs is similar and thus providing further validation of the physiological relevance of the bottom up approach (*12*). Furthermore, because IF assembly and disassembly are regulated by phosphorylation and other posttranslational modifications (*18*), it will be interesting to investigate whether these modifications alter the axial repeat of IFs, reflecting changes in their structural organization. In vitro work already showed that phosphorylation of vimentin by adenosine 3′,5′-monophosphate–dependent protein kinase A soften the filaments (*44*). Moreover, it would be also relevant to determine whether other IF types, such as keratins or neurofilaments, also have an axial repeat and also unfold their α helices cooperatively during filament stretching. Recent in vitro work showed that keratin filaments have different mechanical properties than vimentin and that keratin subunit might slide past each other upon stretching unlike vimentin (*45*). These results, added to fact that keratin filaments are made of ULF with only four tetramers per filament cross section (*46*), suggest that keratin and vimentin filaments have different structural organizations. Because the vimentin rod domain is clearly shorter than that of keratins, we expect keratins to have longer axial repeats than vimentin, as also predicted by theoretical modeling (*43*). The difference between keratins and vimentin molecular organization could explain why the two types of filaments form disjoint networks that cannot copolymerize (*7*, *43*). On the contrary, as vimentin, nestin, and glial fibrillary acidic protein (GFAP) have been shown to copolymerize at the level of single filament (*47*, *48*) and to form heteropolymers (*49*, *50*), we expect GFAP and nestin to display a similar axial repeat as vimentin.

IFs have the unique ability to reversibly elongate along their length (*14*–*17*). In particular, Block *et al.* (*16*) used double optical trapping of individual purified filaments to probe their viscoelastic properties. They showed that although the filament stretching was reversible, vimentin filaments mechanical properties change after stretching, displaying stretch softening (*16*). Their theoretical modeling, combined with stochastic simulations, suggested that the dependence of mechanical properties on deformation history may result from the unfolding of α helices in the rod domain. Our results provide further experimental evidence that it is indeed conformational changes that are responsible for the stretchability of vimentin IFs. By stretching isolated filaments attached to an elastic subtract via antibodies, we observed an increase in the axial repeat, which corresponds to the distance between consecutive tail domains. However, the aspect ratio of the Spots, which corresponds to the intertwined tail domains, is the same without or with stretching, indicating that the tails remain together. These results suggest that the mechanical reorganization within ULF occurs within the rod domains and not within the intertwined regions. Therefore, the molecular mechanism involving unfolding of α helices is more likely than sliding of individual vimentin tetramers, which would lead to a disordering/dislocation of ULFs and degradation of the axial repeat. Moreover, this model is compatible with the reversibility of filament elongation with force (*14*–*17*). However, live SRM with repeated cycles of

strain will be required to further investigate the molecular mechanism responsible for the tensile memory of vimentin IFs.

Although the vimentin network is known to protect cells from large deformations (*5*), we found that vimentin filaments were not extended inside MEF cells for up to 50% amplitude of cell stretching. Instead, filaments reoriented along the stretch axis, with a mechanism that may implicate interaction with other cytoskeletal elements (*47*). This lack of elongation is intriguing because similar stretching amplitudes had a stronger impact on other structures, triggering disassembly of caveolae (*51*) or ruptures in actin stress fibers (*29*). Furthermore, 4 to 10% stretch was sufficient to trigger mechanosensing and mechanotransduction in integrin-based adhesion and to trigger active remodeling of the actin cytoskeleton, which deform and recruit proteins in mechanosensitive structures (*29*). One possible explanation is that vimentin filaments are not under tension before stretching. The requirement to stretch filaments is that longitudinal forces are exerted on at least two positions and that the filaments are already under tension. If the force is applied to only one position, for example, via connection to integrin-based adhesions (*31*), then they will not be extended. If the force is applied to more than one position but the filaments are folded or fluctuate between the positions where the force is applied, then stretching will first lead to pulling out the slack in the filaments before extension along their length. However, although we did not observe an axial repeat increase on average, we cannot exclude that a small fraction of the filaments was stretched locally. In this case, this local stretching would have a limited contribution to the overall pairwise distances parallel to the stretch axis. The other explanation is that IF mechanical connections within the cells are slipping, quickly releasing the tension during the stretch. Thus, our results illustrate the fact that vimentin filaments participate in mechanical energy dissipation during 50% cell stretching, behaving as stress absorbers (*5*). These mechanical properties may also be relevant to other types of IFs such as desmin, another type III IF protein found in highly deformable muscle cells (*7*), or keratins that protect epithelial cells from damage or stress (*4*). More work will be also necessary to understand how the force applied during cell stretching is propagated to cytoplasmic IFs.

In conclusion, the description of the vimentin structural organization by SRM is a powerful tool to investigate the molecular mechanisms involved in filament assembly and response to mechanical strain. In the future, it will be interesting to investigate quantitatively to what extent the size of the axial repeat scales with the tension applied on the filaments and to explore in more detail the coordination between the different subunits within filaments, both in vitro and in cells. Since cells are subjected to complex deformation history, it will be also important to apply more complex stretching patterns with controlled amplitudes, frequencies, and durations. Moreover, testing whether the axial repeat is present in other types of IFs and whether it could be affected by posttranslational modifications (*18*) or IF protein mutations related to diseases (*52*) would be of prime interest. We anticipate that our approach will open the door to new studies aiming at elucidating the role of IFs in cell mechanosensing and, more generally, in cell adaptation to external stimuli.

MATERIALS AND METHODS

Reagents

GFP-nanobodies-AF647 were purchased from Chromotek (#gb2AF647, Planegg-Martinsried, Germany) and Nanotag (FluoTag-X4, #N0304). Spot nanobodies (#etb-250) and GFP-nanobodies-Star635P (#gbas635p) were purchased from Chromotek. Anti-vimentin antibody, monoclonal, clone V9 was purchased from Sigma-Aldrich (catalog no. V6389, St. Louis, MO, USA). Anti-mouse antibody AF647 was purchased from Jackson ImmunoResearch. All the chemicals were purchased from Sigma-Aldrich, except specifically noted.

Labeling of spot nanobodies with Alexa Fluor 647 or Alexa Fluor 594

Spot nanobodies were labeled by Alexa Fluor 647 for dSTORM or Alexa Fluor 594 for STED using an *N*-hydroxysuccinimide ester labeling kit from Molecular Probes (#A37573 and #A37572, respectively) following the protocol provided by the company. The buffer of the nanobodies was changed to 100 mM sodium bicarbonate (pH 8.3) using zeba columns (Thermo Fisher Scientific, Waltham, MA, USA). The amine-reactive dye was dissolved in dimethyl sulfoxide (DMSO) at 10 mg/ml just before use and diluted 10× in the nanobodies solution. After 1 hour of incubation and stirring, the excess of dye was removed using the dye removal column from Pierce (#22858, Thermo Fisher Scientific).

Vimentin constructs

Mouse vimentin-GFP (pEGFP-N3-vimentin) plasmid was given by Pham-Dinh and coworkers (*53*) and described previously. The vimentin constructs (Y117L mutants and addition of a Spot tag) were produced using the Q5 Site-Directed Mutagenesis Kit (catalog no. E0554S, BioLabs) using the primer lists in Table 1. Spot-vimentin-GFP was obtained by addition of a Spot tag [sequence PDRVRAVSHWSS (*37*)] at the N terminus of pEGFP-N3-vimentin. Spot-vimentin was obtained by chopping the GFP at the C-terminal end of the pEGFP-N3-vimentin construct and then adding a Spot tag between the rod and tail domains using linkers made of two amino acids (SG). Vimentin-Spot plasmid for bacterial expression was cloned from the human vimentin wild-type plasmid provided by Herrmann and coworkers (*11*). The cloning procedures strictly followed the protocol provided by BioLabs [polymerase chain reaction (PCR) with the initial construct and the primers written in the table listed below, ligation for 5 min at room temperature, and bacteria transformation]. About four clones were selected per condition and sequenced. The vimentin-HALO construct was obtained after cloning using the HiFi DNA Assembly Cloning Kit (catalog no. E5520S, BioLabs) starting from the tubulin-HALO plasmid (#64691, Addgene) for the vector and the pEGFP-N3-vimentin-GFP construct mentioned above for the insert. The cloning procedure strictly followed the protocol provided by BioLabs (PCR of the vimentin insert, PCR of the HALO vector, ligation with twice more insert than vectors, and then transformation). The primers used are listed in Table 1.

Cell culture and nucleofection

MEF vimentin KO cells described in (*30*) (a gift from H. Herrmann, Deutsches Krebsforschungszentrum, Germany) and the CRISPR cell line U2OS Nup96-SNAP (a gift from J. Ries, European Molecular Biology Laboratory, Heidelberg, Germany) were grown in Dulbecco's modified Eagle's medium (DMEM) with glucose (4.5 g/liter) and supplemented with 10% fetal bovine serum (FBS), 1% penicillin-streptomycin (pen-strep), and 1% nonessential amino acid (NEAA) at 37°C in 5% CO_2. For MEF vimentin KO cells, starting from a 10-cm-diameter petri dish, cells grown to confluence were trypsinized and electroporated with a Nucleofector machine (Lonza).

Table 1. List of primers from cloning the vimentin constructs.

Final plasmid	Initial plasmid	Forward primer	Reverse primer
Spot-vimentin-GFP	Mouse vimentin-GFP [from Pham-Dinh and coworkers (*53*)]	agccattggagcagctccggtTCTACCAGGTCTGTGTCC	cacggcgcgcacgcgcacgcggtctggCATCCTG CCCTTGCCTGA
Vimentin-ΔGFP	Vimentin-GFP	TAAAGCGGCCGCGACTCT	CATGGTGGCGATGGATCC
Vimentin-Spot-Tail ΔGFP	Vimentin-ΔGFP	gtgagccattggagcagcggtagcTCTCTGCCTCTGCCAACC	ggcgcgcacgcggtctgggctaccAATCCTGCTCTCCTCGCC
Spot-vimentin-ΔGFP	Vimentin-ΔGFP	agccattggagcagctccggtTCTACCAGGTCTGTGTCC	cacggcgcgcacgcgcacgcggtctggCATCCTGCCCTTGCCTGA
Vimentin-Δtail ΔGFP	Vimentin-ΔGFP	CAGAATTCTGCAGTCGACG	AATCCTGCTCTCCTCGCC
VimentinΔtail ΔGFP-Spot	Vimentin-Δtail-ΔGFP	GtgagccattggagcagcTAAAGCGGCCGCGACTCT	ggcgcgcacgcggtctggCATGGTGGCGATGGATCC
Vimentin-Y117L	Vimentin-GFP;Vimentin-Spot-Tail-ΔGFP; Spot-vimentin-ΔGFP	CTTTGCCAACctCATCGACAAGGTGC	CGGTCATTCAGCTCCTGC
Vimentin-HALO	tubulin-HALO plasmid (addgene #64691); vimentin-GFP	TTCAAGGTCATCGTGATGCTGAG; agcatcacgatgaccttgaaCAGTCGAACGGCAGCGAAATC	CtgagtgtgtgcaatttttaGCCGGAAATCTCGAGCGTG; TAAAAATTGCACACACTCAGTGCAGC
Vimentin-Spot for bacterial expression	Human vimentin [from Herrmann and coworkers (*11*)]	gccgtgagccattggagcagcTAAAAATTGCACACACTCAG	gcgcacgcggtctggtgatccTTCAAGGTCATCGTGATG

We used 2 μg of DNA, mixed with 97 μl of solution for electroporation (Mirus MIR 50111). After electroporation, cells were resuspended in preheated medium and plated on clean 18-mm #1.5H glass coverslips (Marienfeld) in a 12-well plate with ~3000 cells per well. U373 cells, which are astrocytoma cells, were grown in minimum essential medium (MEM) supplemented with 10% FBS, 1% pen-strep, and 1% NEAAs. DMEM, MEM, pen-strep, NEAA, and FBS were purchased from Gibco.

Drug treatments

Nocodazole was added at a final concentration of 10 μM 1 hour before fixation (stock at 10 mM in DMSO). After 1 hour of incubation with nocodazole, vimentin filaments did not have the time to collapse around the nucleus (*47*). Blebbistatin was used at a final concentration of 2 μM (stock at 10 mM in DMSO) and was also added 1 hour before fixation. Nocodazole was purchased from Calbiochem (San Diego, CA, USA), and blebbistatin was purchased from Sigma-Aldrich.

Fixation and labeling

Twenty-four hours after electroporation, cells were fixed in cold (−20°) methanol for 5 min and blocked with 5% bovine serum albumin (BSA) in phosphate-buffered saline (PBS) for 1 hour. Cells were then incubated for 2 hours with fluorescent nanobodies (dilution, 1/200 in PBS) at room temperature and rinsed three times with PBS for 5 min on an orbital shaker. For immunofluorescence, cells were incubated for 1 hour with anti-vimentin antibodies (dilution, 1/500e in PBS) after blocking, washed three times for 5 min in PBS, and incubated for another hour with anti-mouse Alexa Fluor 647 antibodies (dilution, 1/500 in PBS). After three washes for 5 min in PBS, cells were incubated with 100-nm tetraspeck beads (#T7279, Thermo Fisher Scientific) with a dilution of 1/500 in PBS for 30 min on an orbital shaker at room temperature and then stored at 4° in PBS before use.

Sample preparation and imaging buffer

Eighteen-millimeter 18 mm coverslips are mounted on magnetic sample holders (CM-B18-1, Live Cell Instrument) with 1 ml of imaging buffer and then closed with a lit. The imaging buffer is made of tris-NaCl buffer [50 mM tris and 10 mM NaCl (pH 8)] supplemented with 10% of glucose (100 mg/ml), 10 mM monoethanolamine (MEA), glucose oxidase (0.5 mg/ml; 75 U/ml), and catalase (40 μg/ml; 80 to 200 U/ml). For dSTORM images of vimentin filaments reconstituted in vitro, the concentration of NaCl was increased to 100 mM.

2D dSTORM imaging and processing

2D dSTORM images were acquired on an Elyra Zeiss microscope using the TIRF μ-HD mode that focuses the intensity of the lasers in the center of the field of view, a 100× numerical aperture (NA) 1.46 objective, a 1.6 optovar lens, and a 512 by 512 electron-multiplying charge-coupled device (EMCCD) camera. We worked with 20 μm–by–20 μm field of view, used 15- to 20-ms exposure time, and acquired 20,000 to 40,000 frames at maximal intensity of the 642-nm laser power to pump most of the Alexa Fluor 647 dyes to the dark state (~2 kW/cm^2) as described previously (*54*). Super-resolution images were reconstructed, and drift correction was carried out using the Picasso software available on GitHub as previously described (*24*).

3D dSTORM imaging

We used a homemade microscopy system to perform 3D dSTORM imaging based on a previously published method (*38*). The system consists of two microscopes facing each other, oriented horizontally and organized around the biological sample. The first microscope is composed of (i) a high-NA objective lens (Olympus, UPSALO100×, NA 1.4), (ii) a Semrock -Di01-R405/488/561/635-25×36 quadband dichroic that reflects the excitation laser beam coming from a near infrared laser light (λ = 642 nm; Oxxius LBX series) and filters the fluorescence light coming from the sample, (iii) a tube lens composed of an achromatic doublet (f = 250 mm; AC508-250-A-ML, Thorlabs), and a 4f system composed of two achromatic doublet lenses (f = 100 mm; AC254-100-A-ML, Thorlabs) used to image the biological sample on the ship of an EMCCD camera (CAM1, 512 pixel–by–512 pixel Andor Ixon 897). In the intermediate plane of the 4f system, a cylindrical lens (f = 1 m; LJ1516RM-A, Thorlabs) is added, modifying the shape of the point spread function. Long-pass and band-pass filters Semrock (long-wave pass 647 and FF01-676/29) are added in front of the camera to filter out residual photons from the laser. The second microscope is identical to the first one, balancing the number of photons collected.

The biological sample is sandwiched between two high-resolution coverslips (#1.5H, 224 mm by 50 mm, Marienfield), which are placed between the two objective lenses and held on a homemade 3D sample holder. Fluorescent beads are added to the biological sample to help select the same focal plane with both microscopes and to correct a posteriori the 3D spatial drift.

Once the focal plane is selected in the biological sample with the both microscopes, several tens of thousands of 60 μm–by–60 μm images are acquired by the two synchronized cameras. Because of the geometry of the system, the astigmatic point spread function (PSFs) are oriented at 90° from each other on both cameras. Single molecules appearing in successive images are localized with Zernike Optimized Localization approach 3D (ZOLA-3D) (*55*). This algorithm allows the correction of 3D spatial drift using fiducial markers and has been adapted to this imaging system. Optionally, ZOLA-3D can correct for subpixel displacements between the images acquired by the two cameras, and a specific model has been developed to create a localization table combining the astigmatic PSFs acquired in both cameras ensuring the best localization accuracy.

STED imaging

STED images were acquired on a STEDYCON microscope, and an expert line microscope from Abberior Instruments GmbH, using the adaptive illumination technology reducing laser illumination of the sample (around 5× to 10×). Spot-vimentin-Y117L-GFP proteins were labeled with GFP-nanobodies-Star635P and Spot-nanobodies-AF594, following the protocol described above.

In vitro reconstitution of vimentin-Spot filaments

Vimentin-Spot protein was purified from bacteria as described previously (*40*). Briefly, vimentin-Spot was expressed in BL21 star (Sigma-Aldrich) in Terrific Broth medium overnight at 37° after induction at an optical density (O.D.) of 1.2. After centrifugation, bacteria were lysed with lysozyme in the presence of deoxyribonuclease (Roche), ribonuclease (Roche), and protein inhibitors [pefabloc and phenylmethylsulfonyl fluoride (PMSF)]. Inclusion bodies were collected and washed five times by successive steps of centrifugation and resuspension using a cooled douncer. After the last washing step, inclusion bodies were resuspended in a denaturing buffer [8 M urea, 5 mM tris (pH 7.5), 1 mM EDTA, 1 mM dithiothreitol (DTT), and 1% PMSF] and centrifuged at high speed (100,000*g*) for 1 hour. Starting from the supernatant, vimentin-Spot purification was obtained after two steps of exchange chromatography, using, first, an anionic column (DEAE Sepharose, GE Healthcare) and then a cationic column (CM Sepharose, GE Healthcare). The protein was collected in 2-ml tubes, and the concentration was monitored by Bradford. The most concentrated fractions were pooled together and stored at −80° with additional 10 mM methylamine hydrochloride solution. Vimentin-Spot proteins were renatured after stepwise dialysis (8, 6, 4, 2, 1, and 0 M urea) into sodium phosphate buffer (2.5 mM, pH 7) supplemented with 1 mM DTT, using dialysis tubing (SERVAPOR; cutoff at 12 kDa). Each step lasted 15 to 30 min, except the last dialysis performed overnight at 4° with 2 liters of buffer. Filament assembly was triggered by addition of 100 mM KCl (final) to a solution of renaturated vimentin-Spot at 0.2 mg/ml, and elongation was performed by incubation at 37° for 3 hours for long filaments and 2 s to obtain ULFs.

Transmission EM imaging of reconstituted filaments

Vimentin-Spot filaments were grown at 0.2 mg/ml for 3 hours at 37° after addition of 100 mM KCl and then fixed with an equal volume of 0.5% glutaraldehyde in a sodium phosphate buffer (2.5 mM) supplemented with 100 mM KCl. Four microliters of the sample was spotted on a carbon-coated grid primarily glow discharged and incubated at room temperature for 1 min. Uranyl acetate (2%) in water was used to contrast the grids and incubated for 1 min. The grid was then dried and observed under 120 kV using a Tecnai microscope (Thermo Fisher Scientific) and imaged using a 4000 by 4000 Eagle camera (Thermo Fisher Scientific).

Stretching experiments coupled to DNA-PAINT and imaging vimentin-HALO in cells

The stretching device and its coupling to DNA-PAINT were previously described (*29*). Briefly, a plasma-cleaned PDMS sheet (10 μm; Sylgard 184, DE9330, Samaro) was deposited on a plasma-cleaned glass coverslip, lubricated by a thin layer of low-viscous glycerol, and reinforced by a thicker PDMS elastomer frame. The uniaxial stretch was applied thanks to a 3D printed device consisting of a fixed holding arm and a mobile arm connected to a piezo-electric motor (M-663 Linear Positioning Stage, PI). PDMS substrate was coated with human fibronectin for 90 min at 37°. Then, 18 hours after electroporation with a mix of vimentin-HALO:vimentin-GFP (9:1), MEF vimentin KO cells were plated on the stretching device and spread for 3 hours at 37°C. The device was mounted onto the microscope at 37°C to acquire low-resolution vimentin-GFP images of cells before stretching. Then, at room temperature and outside the microscope, a single uniaxial stretch of 30 or 50% was applied with a speed of 0.5 mm/s and a duration of 5 or 10 s, respectively, followed by rapid cell fixation in 4% paraformaldehyde, 0.3% Triton X-100, and 0.3% glutaraldehyde in PBS buffer for 20 min at 37°. Simultaneously, the stretching arm was clamped to the fixed arm using a thread and groove system to maintain the stretching throughout the subsequent labeling and imaging steps. Then, cells were then blocked for 90 min with 3% BSA in PBS and incubated with the HALO-PAINT probe for 15 min. Back on the microscope, we located the cell imaged before stretching and acquired low-resolution images of vimentin-GFP after stretching. Then, super-resolution imaging was performed. Cells were imaged at 25°C in the stretching device with

an inverted motorized microscope (Nikon Ti) equipped with a CFI Apochromat TIRF 100× oil, NA 1.49 objective, and a perfect focus system, allowing long acquisition in TIRF illumination mode. For DNA-PAINT microscopy, cells expressing vimentin-HALO were first incubated with 90-nm gold nanoparticles (Cytodiagnostics) to serve as fiducial markers. Vimentin-HALO was visualized with Cy3B-labeled DNA imager strands added to the stretching chamber at variable concentrations (2 to 5 nM) using a streaming mode at 6.7 Hz. Cy3B-labeled strands were visualized with a 561-nm laser (Cobolt Jive). Fluorescence was collected by the combination of a dichroic filter and emission filters (dichroic, Di01-R561; emission, FF01-617/73; Semrock) and a sensitive scientific complementary metal-oxide semiconductor (ORCA-Flash4.0, Hammamatsu). The acquisition was steered by MetaMorph software (Molecular Devices) in streaming mode at 6.7 Hz. Vimentin-GFP was imaged using a conventional GFP filter cube (excitation, FF01-472/30; dichroic, FF-495Di02; emission, FF02-520/28; Semrock). DNA-PAINT image reconstruction and drift correction were carried out using the Picasso software (*24*).

Stretching experiments coupled to 2D dSTORM imaging reconstituted vimentin-Spot filaments

Using the same stretching device and microscope setup described above, the thin plasma-cleaned PDMS layer was incubated with vimentin antibodies [concentration, 0.2 mg/ml; sc-6260, Santa Cruz Biotechnology (V9)] with a dilution of 1/10 in buffer V [2.5 mM sodium phosphate (pH 7) and 100 mM KCl] for 15 min, rinsed with buffer V, incubated with a mix of vimentin-Spot filaments diluted 50 times, tetraspeck beads diluted 500 times, and Spot-nanobodies-AF647 diluted 1000× in buffer V for 3 hours. Then, the stretching chamber was rinsed with STORM buffer and filled with 2 ml of STORM buffer freshly prepared and changed every 30 min. A single uniaxial stretch of 30% was applied with a speed of 0.03 mm/s and a total duration of 1 min.

ULF pairwise distance analysis

For 2D measurements, first, the ULFs were detected in low-resolution images by thresholding. Then, for the isolated ULF dots, which contained only two peaks in the super-resolution images, intensity profiles were plotted along a thick line (5 pixels of 5 nm) containing the two peaks, and the distance of the peaks, called pairwise distance, was quantified using a double Gaussian fit.

For 3D measurements, the beginning of the procedure is the same. ULFs are detected from low-resolution images by thresholding. We analyzed the ULFs when two peaks were present within the ULF dots in the 2D projection of the 3D super-resolved stack. A transverse section was plotted along the doublet (as shown in Fig. 1G, side view). The pairwise distance was calculated as the distance between the centroids within the side view. Note that when ULFs are close to being vertical, the 2D projection of the pairwise distance goes below the resolution of technique (~25 nm) and is therefore not detected. The tilt angles of ULFs close to 90° are therefore underestimated with this method.

Filament pairwise distance analysis

Analysis of the double length was performed using MATLAB (MathWorks) and Fiji and involved several steps depicted in Fig. 3C: (1) isolating filaments, (2) detecting single vimentin peaks and linking them to their two nearest neighbors, (3) removing graph nodes that have four edges or more, (4) resolving triplets, (5) removing the connected components that have fewer than four nodes, and (6) measuring distances from the remaining edges.

1) Isolating filaments. The reconstructed super-resolution image of vimentin contains spurious signals away from filaments that we need to filter out. Because true vimentin peaks on filaments are spaced by a distance smaller than the filament persistence length, we can use filter operations to yield a broad mask that contains only the filaments. To do so, we used the tubeness filter present in Fiji (*56*, *57*), with a σ value larger than the peak separation but smaller than the filament persistence length would work. We picked σ = 12 pixels. We then thresholded the tubeness image and segmented it into individual regions. We rejected regions with an area smaller than 1000 pixels and with an aspect ratio larger than 0.5. The resulting mask delineates individual filaments. Some high-curvature filament locations were also filtered out by this method.

2) Detecting single vimentin peaks and linking them to their two nearest neighbors. In the resulting image, a single vimentin peak is made of possibly several bright Spots clustered around the vimentin peak location. We tried several approaches to yielding the vimentin peaks location from individual Spots. We first tried using the DBSCAN algorithm on the emitter locations directly, as first proposed in Endesfelder *et al.* (*58*) and with an improved implementation proposed in Tran *et al.* (*59*) and Truan *et al.* (*60*) to harness close clusters. However, in our case, the number of individual Spots per vimentin peak appears too small to achieve satisfactory results. Individual clusters bridge over several vimentin peaks. We therefore turned to direct analysis of the reconstructed super-resolution image. We lastly settled to harvest peak locations by directly detecting local maxima in the reconstructed image, filtering for the brightest ones and refining their location using a simple centroid calculation over 5 by 5 pixels. We then built a simple undirected graph connecting all vimentin peaks closer than 150 nm and used it to further filter out spurious peaks.

3) Removing graph nodes that have four edges or more. Ideally, the graph would be made of long connected components corresponding to filaments, with each vimentin peak having one or two connections to the neighbor. However, filaments can cross, and spurious detections complicate the analysis. We first filtered out all peaks that have four or more connections to neighbor peaks (quadruplets). Some peaks had three or more connections (triplets), which we tried to resolve in the following manner.

4) Resolving triplets. A peak with three connections to three neighbor peaks corresponds to three candidate doublets. We look for the angles between each doublet pair. If the doublets are not roughly aligned, that is, their angle is below 130° and above −130°, then they make a sharp nick. We then vote against these two doublets. We do this for all the possible doublet pairs (three combinations are possible). In addition, in the end, we look whether there is a doublet that was voted against twice. This is the doublet that is not aligned with the roughly straight line built by the two others. We then remove it. If there is no such doublet (the three of them have zero votes because they are all roughly aligned), then we simply remove the longest one.

5) Removing the connected components that have fewer than four nodes. The remaining peaks all have one or two connections to neighbor peaks. In the graph, they build several connected components representing parts of individual filaments. Some components are just made of a few peaks, for which defining a global orientation is hard. If such a component is made of less than four nodes, then we remove it.

6) Measuring distances from the remaining edges. The remaining edges in the graph correspond to single vimentin doublets, belonging to long filament parts, from which we extract the doublet length. In a typical image used in this analysis (DNA-PAINT as shown in Fig. 3), we find 38,890 peaks in step (2) of which we keep only the 29,524 brightest. From them, we build a graph made of 29,524 nodes and 28,379 edges. By filtering out quadruplets, we remove 413 peaks. By curating the triplets, we remove 5502 edges. By removing the filament parts smaller than four nodes, we remove 10,797 peaks. In the end, we are left with 18,314 peaks and 15,422 doublets, from which we yield 15,422 pairwise distance measurements.

Statistical analysis

All experiments were repeated at least three times except specifically mentioned. The statistical analyses were performed using GraphPad. *P* values were calculated using a nested *t* test of the three repeats for Figs. 1 (D to J) and 2C and a paired *t* test for Fig. 3E. A *P* value below 0.05 was considered as statistically significant. $^{*}P < 0.05$, $^{**}P < 0.01$, $^{***}P < 0.001$, and $^{****}P < 0.0001$.

SUPPLEMENTARY MATERIALS

Supplementary material for this article is available at https://science.org/doi/10.1126/sciadv.abm2696

View/request a protocol for this paper from *Bio-protocol*.

REFERENCES AND NOTES

1. F. Huber, A. Boire, M. P. Lopez, G. H. Koenderink, Cytoskeletal crosstalk: When three different personalities team up. *Curr. Opin. Cell Biol.* **32**, 39–47 (2015).
2. S. Duarte, A. Viedma-Poyatos, E. Navarro-Carrasco, A. E. Martinez, M. A. Pajares, D. Perez-Sala, Vimentin filaments interact with the actin cortex in mitosis allowing normal cell division. *Nat. Commun.* **10**, 4200 (2019).
3. M. P. Serres, M. Samwer, B. A. Truong Quang, G. Lavoie, U. Perera, D. Gorlich, G. Charras, M. Petronczki, P. P. Roux, E. K. Paluch, F-actin interactome reveals vimentin as a key regulator of actin organization and cell mechanics in mitosis. *Dev. Cell* **52**, 210–222.e7 (2020).
4. E. Latorre, S. Kale, L. Casares, M. Gomez-Gonzalez, M. Uroz, L. Valon, R. V. Nair, E. Garreta, N. Montserrat, A. Del Campo, B. Ladoux, M. Arroyo, X. Trepat, Active superelasticity in three-dimensional epithelia of controlled shape. *Nature* **563**, 203–208 (2018).
5. J. Hu, Y. Li, Y. Hao, T. Zheng, S. K. Gupta, G. A. Parada, H. Wu, S. Lin, S. Wang, X. Zhao, R. D. Goldman, S. Cai, M. Guo, High stretchability, strength, and toughness of living cells enabled by hyperelastic vimentin intermediate filaments. *Proc. Natl. Acad. Sci. U.S.A.* **116**, 17175–17180 (2019).
6. E. Lazarides, Intermediate filaments as mechanical integrators of cellular space. *Nature* **283**, 249–256 (1980).
7. H. Herrmann, U. Aebi, Intermediate filaments: Structure and assembly. *Cold Spring Harb. Perspect. Biol.* **8**, a018242 (2016).
8. J. Ngai, T. R. Coleman, E. Lazarides, Localization of newly synthesized vimentin subunits reveals a novel mechanism of intermediate filament assembly. *Cell* **60**, 415–427 (1990).
9. G. Colakoglu, A. Brown, Intermediate filaments exchange subunits along their length and elongate by end-to-end annealing. *J. Cell Biol.* **185**, 769–777 (2009).
10. B. Noding, H. Herrmann, S. Koster, Direct observation of subunit exchange along mature vimentin intermediate filaments. *Biophys. J.* **107**, 2923–2931 (2014).
11. N. Mucke, T. Wedig, A. Burer, L. N. Marekov, P. M. Steinert, J. Langowski, U. Aebi, H. Herrmann, Molecular and biophysical characterization of assembly-starter units of human vimentin. *J. Mol. Biol.* **340**, 97–114 (2004).
12. A. A. Chernyatina, D. Guzenko, S. V. Strelkov, Intermediate filament structure: The bottom-up approach. *Curr. Opin. Cell Biol.* **32**, 65–72 (2015).
13. K. N. Goldie, T. Wedig, A. K. Mitra, U. Aebi, H. Herrmann, A. Hoenger, Dissecting the 3-D structure of vimentin intermediate filaments by cryo-electron tomography. *J. Struct. Biol.* **158**, 378–385 (2007).
14. Z. Qin, L. Kreplak, M. J. Buehler, Hierarchical structure controls nanomechanical properties of vimentin intermediate filaments. *PLoS One* **4**, e7294 (2009).
15. J. Block, H. Witt, A. Candelli, E. J. Peterman, G. J. Wuite, A. Janshoff, S. Koster, Nonlinear loading-rate-dependent force response of individual vimentin intermediate filaments to applied strain. *Phys. Rev. Lett.* **118**, 048101 (2017).
16. J. Block, H. Witt, A. Candelli, J. C. Danes, E. J. G. Peterman, G. J. L. Wuite, A. Janshoff, S. Koster, Viscoelastic properties of vimentin originate from nonequilibrium conformational changes. *Sci. Adv.* **4**, eaat1161 (2018).
17. J. Forsting, J. Kraxner, H. Witt, A. Janshoff, S. Koster, Vimentin intermediate filaments undergo irreversible conformational changes during cyclic loading. *Nano Lett.* **19**, 7349–7356 (2019).
18. N. T. Snider, M. B. Omary, Post-translational modifications of intermediate filament proteins: Mechanisms and functions. *Nat. Rev. Mol. Cell Biol.* **15**, 163–177 (2014).
19. L. Schermelleh, A. Ferrand, T. Huser, C. Eggeling, M. Sauer, O. Biehlmaier, G. P. C. Drummen, Super-resolution microscopy demystified. *Nat. Cell Biol.* **21**, 72–84 (2019).
20. M. Lelek, M. T. Gyparaki, G. Beliu, F. Schueder, J. Griffié, S. Manley, R. Jungmann, M. Sauer, M. Lakadamyali, C. Zimmer, Single-molecule localization microscopy. *Nature Reviews Methods Primers* **1**, 39 (2021).
21. E. Betzig, G. H. Patterson, R. Sougrat, O. W. Lindwasser, S. Olenych, J. S. Bonifacino, M. W. Davidson, J. Lippincott-Schwartz, H. F. Hess, Imaging intracellular fluorescent proteins at nanometer resolution. *Science* **313**, 1642–1645 (2006).
22. M. J. Rust, M. Bates, X. Zhuang, Sub-diffraction-limit imaging by stochastic optical reconstruction microscopy (STORM). *Nat. Methods* **3**, 793–795 (2006).
23. M. Heilemann, S. van de Linde, M. Schuttpelz, R. Kasper, B. Seefeldt, A. Mukherjee, P. Tinnefeld, M. Sauer, Subdiffraction-resolution fluorescence imaging with conventional fluorescent probes. *Angew. Chem. Int. Ed. Engl.* **47**, 6172–6176 (2008).
24. J. Schnitzbauer, M. T. Strauss, T. Schlichthaerle, F. Schueder, R. Jungmann, Super-resolution microscopy with DNA-PAINT. *Nat. Protoc.* **12**, 1198–1228 (2017).
25. K. I. Willig, S. O. Rizzoli, V. Westphal, R. Jahn, S. W. Hell, STED microscopy reveals that synaptotagmin remains clustered after synaptic vesicle exocytosis. *Nature* **440**, 935–939 (2006).
26. P. Kanchanawong, G. Shtengel, A. M. Pasapera, E. B. Ramko, M. W. Davidson, H. F. Hess, C. M. Waterman, Nanoscale architecture of integrin-based cell adhesions. *Nature* **468**, 580–584 (2010).
27. O. Rossier, V. Octeau, J. B. Sibarita, C. Leduc, B. Tessier, D. Nair, V. Gatterdam, O. Destaing, C. Albiges-Rizo, R. Tampe, L. Cognet, D. Choquet, B. Lounis, G. Giannone, Integrins β1 and β3 exhibit distinct dynamic nanoscale organizations inside focal adhesions. *Nat. Cell Biol.* **14**, 1057–1067 (2012).
28. A. Szymborska, A. de Marco, N. Daigle, V. C. Cordes, J. A. Briggs, J. Ellenberg, Nuclear pore scaffold structure analyzed by super-resolution microscopy and particle averaging. *Science* **341**, 655–658 (2013).
29. S. Massou, F. Nunes Vicente, F. Wetzel, A. Mehidi, D. Strehle, C. Leduc, R. Voituriez, O. Rossier, P. Nassoy, G. Giannone, Cell stretching is amplified by active actin remodelling to deform and recruit proteins in mechanosensitive structures. *Nat. Cell Biol.* **22**, 1011–1023 (2020).
30. M. Meier, G. P. Padilla, H. Herrmann, T. Wedig, M. Hergt, T. R. Patel, J. Stetefeld, U. Aebi, P. Burkhard, Vimentin coil 1A-A molecular switch involved in the initiation of filament elongation. *J. Mol. Biol.* **390**, 245–261 (2009).
31. M. Gregor, S. Osmanagic-Myers, G. Burgstaller, M. Wolfram, I. Fischer, G. Walko, G. P. Resch, A. Jörgl, H. Herrmann, G. Wiche, Mechanosensing through focal adhesion-anchored intermediate filaments. *FASEB J.* **28**, 715–729 (2014).
32. A. Robert, M. J. Rossow, C. Hookway, S. A. Adam, V. I. Gelfand, Vimentin filament precursors exchange subunits in an ATP-dependent manner. *Proc. Natl. Acad. Sci. U.S.A.* **112**, E3505–E3514 (2015).
33. J. Ries, C. Kaplan, E. Platonova, H. Eghlidi, H. Ewers, A simple, versatile method for GFP-based super-resolution microscopy via nanobodies. *Nat. Methods* **9**, 582–584 (2012).
34. J. V. Thevathasan, M. Kahnwald, K. Cieslinski, P. Hoess, S. K. Peneti, M. Reitberger, D. Heid, K. C. Kasuba, S. J. Hoerner, Y. Li, Y. L. Wu, M. Mund, U. Matti, P. M. Pereira, R. Henriques, B. Nijmeijer, M. Kueblbeck, V. J. Sabinina, J. Ellenberg, J. Ries, Nuclear pores as versatile reference standards for quantitative superresolution microscopy. *Nat. Methods* **16**, 1045–1053 (2019).
35. H. Herrmann, M. Haner, M. Brettel, S. A. Muller, K. N. Goldie, B. Fedtke, A. Lustig, W. W. Franke, U. Aebi, Structure and assembly properties of the intermediate filament protein vimentin: The role of its head, rod and tail domains. *J. Mol. Biol.* **264**, 933–953 (1996).
36. N. Mucke, L. Kreplak, R. Kirmse, T. Wedig, H. Herrmann, U. Aebi, J. Langowski, Assessing the flexibility of intermediate filaments by atomic force microscopy. *J. Mol. Biol.* **335**, 1241–1250 (2004).
37. D. Virant, B. Traenkle, J. Maier, P. D. Kaiser, M. Bodenhofer, C. Schmees, I. Vojnovic, B. Pisak-Lukats, U. Endesfelder, U. Rothbauer, A peptide tag-specific nanobody enables high-quality labeling for dSTORM imaging. *Nat. Commun.* **9**, 930 (2018).
38. K. Xu, H. P. Babcock, X. Zhuang, Dual-objective STORM reveals three-dimensional filament organization in the actin cytoskeleton. *Nat. Methods* **9**, 185–188 (2012).
39. A. Robert, H. Herrmann, M. W. Davidson, V. I. Gelfand, Microtubule-dependent transport of vimentin filament precursors is regulated by actin and by the concerted action of Rho- and p21-activated kinases. *FASEB J.* **28**, 2879–2890 (2014).

40. H. Herrmann, L. Kreplak, U. Aebi, Isolation, characterization, and in vitro assembly of intermediate filaments. *Methods Cell Biol.* **78**, 3–24 (2004).
41. M. E. Brennich, U. Vainio, T. Wedig, S. Bauch, H. Herrmann, S. Koster, Mutation-induced alterations of intra-filament subunit organization in vimentin filaments revealed by SAXS. *Soft Matter* **15**, 1999–2008 (2019).
42. F. Balzarotti, Y. Eilers, K. C. Gwosch, A. H. Gynna, V. Westphal, F. D. Stefani, J. Elf, S. W. Hell, Nanometer resolution imaging and tracking of fluorescent molecules with minimal photon fluxes. *Science* **355**, 606–612 (2017).
43. P. M. Steinert, L. N. Marekov, D. A. Parry, Diversity of intermediate filament structure. Evidence that the alignment of coiled-coil molecules in vimentin is different from that in keratin intermediate filaments. *J. Biol. Chem.* **268**, 24916–24925 (1993).
44. J. Kraxner, C. Lorenz, J. Menzel, I. Parfentev, I. Silbern, M. Denz, H. Urlaub, B. Schwappach, S. Koster, Post-translational modifications soften vimentin intermediate filaments. *Nanoscale* **13**, 380–387 (2021).
45. C. Lorenz, J. Forsting, A. V. Schepers, J. Kraxner, S. Bauch, H. Witt, S. Klumpp, S. Koster, Lateral subunit coupling determines intermediate filament mechanics. *Phys. Rev. Lett.* **123**, 188102 (2019).
46. H. Herrmann, M. Haner, M. Brettel, N. O. Ku, U. Aebi, Characterization of distinct early assembly units of different intermediate filament proteins. *J. Mol. Biol.* **286**, 1403–1420 (1999).
47. C. Leduc, S. Etienne-Manneville, Regulation of microtubule-associated motors drives intermediate filament network polarization. *J. Cell Biol.* **216**, 1689–1703 (2017).
48. C. Eliasson, C. Sahlgren, C. H. Berthold, J. Stakeberg, J. E. Celis, C. Betsholtz, J. E. Eriksson, M. Pekny, Intermediate filament protein partnership in astrocytes. *J. Biol. Chem.* **274**, 23996–24006 (1999).
49. R. A. Quinlan, W. W. Franke, Molecular interactions in intermediate-sized filaments revealed by chemical cross-linking. Heteropolymers of vimentin and glial filament protein in cultured human glioma cells. *Eur. J. Biochem.* **132**, 477–484 (1983).
50. P. M. Steinert, Y. H. Chou, V. Prahlad, D. A. Parry, L. N. Marekov, K. C. Wu, S. I. Jang, R. D. Goldman, A high molecular weight intermediate filament-associated protein in BHK-21 cells is nestin, a type VI intermediate filament protein. Limited co-assembly in vitro to form heteropolymers with type III vimentin and type IV α-internexin. *J. Biol. Chem.* **274**, 9881–9890 (1999).
51. B. Sinha, D. Koster, R. Ruez, P. Gonnord, M. Bastiani, D. Abankwa, R. V. Stan, G. Butler-Browne, B. Vedie, L. Johannes, N. Morone, R. G. Parton, G. Raposo, P. Sens, C. Lamaze, P. Nassoy, Cells respond to mechanical stress by rapid disassembly of caveolae. *Cell* **144**, 402–413 (2011).
52. S. V. Strelkov, H. Herrmann, U. Aebi, Molecular architecture of intermediate filaments. *Bioessays* **25**, 243–251 (2003).
53. C. Mignot, C. Delarasse, S. Escaich, B. Della Gaspera, E. Noe, E. Colucci-Guyon, C. Babinet, M. Pekny, P. Vicart, O. Boespflug-Tanguy, A. Dautigny, D. Rodriguez, D. Pham-Dinh, Dynamics of mutated GFAP aggregates revealed by real-time imaging of an astrocyte model of Alexander disease. *Exp. Cell Res.* **313**, 2766–2779 (2007).
54. C. Leduc, A. Salles, S. L. Shorte, S. Etienne-Manneville, Imaging intermediate filaments and microtubules with 2-dimensional direct stochastic optical reconstruction microscopy. *J Vis. Exp.*, 57087 (2018).
55. A. Aristov, B. Lelandais, E. Rensen, C. Zimmer, ZOLA-3D allows flexible 3D localization microscopy over an adjustable axial range. *Nat. Commun.* **9**, 2409 (2018).
56. J. Schindelin, I. Arganda-Carreras, E. Frise, V. Kaynig, M. Longair, T. Pietzsch, S. Preibisch, C. Rueden, S. Saalfeld, B. Schmid, J. Y. Tinevez, D. J. White, V. Hartenstein, K. Eliceiri, P. Tomancak, A. Cardona, Fiji: An open-source platform for biological-image analysis. *Nat. Methods* **9**, 676–682 (2012).
57. Y. Sato, S. Nakajima, N. Shiraga, H. Atsumi, S. Yoshida, T. Koller, G. Gerig, R. Kikinis, Three-dimensional multi-scale line filter for segmentation and visualization of curvilinear structures in medical images. *Med. Image Anal.* **2**, 143–168 (1998).
58. U. Endesfelder, K. Finan, S. J. Holden, P. R. Cook, A. N. Kapanidis, M. Heilemann, Multiscale spatial organization of RNA polymerase in Escherichia coli. *Biophys. J.* **105**, 172–181 (2013).
59. T. Tran, K. Drab, M. Daszykowski, Revised DBSCAN algorithm to cluster data with dense adjacent clusters. *Chemom. Intel. Lab. Syst.* **120**, 92–96 (2013).
60. Z. Truan, L. Tarancon Diez, C. Bonsch, S. Malkusch, U. Endesfelder, M. Munteanu, O. Hartley, M. Heilemann, A. Furstenberg, Quantitative morphological analysis of arrestin2 clustering upon G protein-coupled receptor stimulation by super-resolution microscopy. *J. Struct. Biol.* **184**, 329–334 (2013).

Acknowledgments: We thank R. Leube and R. Windoffer from the University of Aachen, P. Nassoy from University of Bordeaux, M. Lenz from University of Orsay, and B. Boëda, V. Roca, B. Lelandais, C. Weber, and T. Obadia from Institut Pasteur for discussions; and D. Pham-Dinh, J. Ries, and H. Herrmann for reagents. We thank F. Eghiaian, J. Hanne, and J.-G. Schloetel from Abberior Instruments GmbH for imaging our samples. C. Leduc thanks H. Herrmann and his group for teaching the techniques involved in vimentin purification and the support of the EU-supported Cooperation in Science and Technology (COST) action NANONET (Nanomechanics of intermediate filament networks). **Funding:** We acknowledge A. Salles and the Imagopole of Institut Pasteur (Paris), and the financial support of the Institut Pasteur (Paris), the France–BioImaging infrastructure network supported by the French National Research Agency (ANR-10-INSB-04, Investments for the future), and the Région Ile-de-France (program DIM-Malinf) for the use of the Elyra microscope and for funding the development of a dual-objective STORM system ("NANOINF" project to C.Z.). This work was supported by the French National Research Agency: ANR-16-CE13-0019 (to C.L.), ANR-18-CE13-0026 (to G.G.), ANR-21-CE11-0004-01 (to C.L and G.G.), and ANR-16-CE92-0034 (to G.G.); the Ligue contre le cancer EL2017.LNCC (to S.E.-M.); and the Centre National de la Recherche Scientifique and Institut Pasteur. **Author contributions:** C.L. conceived and coordinated the project. C.L., G.G., S.E.-M., C.Z., F.N.V., and M.L. designed the research. F.N.V. performed and analyzed the experiments combining cell stretching and SRM. M.L. performed and analyzed the experiments with the dual-objective microscopy setup. J.-Y.T. wrote the software for the automatic analysis of pairwise distances along filaments. G.P.-A. performed EM imaging. C.L. performed and analyzed 2D dSTORM imaging and cloned the vimentin constructs. Q.D.T. purified, labeled vimentin, and prepared purified vimentin filaments. C.L. and G.G. wrote the manuscript with input from all authors. **Competing interests:** The authors declare that they have no competing interests. **Data and materials availability:** All data needed to evaluate the conclusions in the paper are present in the paper and/or the Supplementary Materials. The U2OS Nup96-SNAP cell line used in fig. S5 can be provided by J. Ries pending scientific review and a completed material transfer agreement.

Submitted 6 September 2021
Accepted 11 January 2022
Published 25 February 2022
10.1126/sciadv.abm2696